INSTITUTE OF PHYSICS PUBLISHING PHYSICS IN MEDICINE AND BIOLOGY

Phys. Med. Biol. **49** (2004) 2733–2752 PII: S0031-9155(04)71781-9

Half-scan and single-plane intensity diffraction tomography for phase objects

Daxin Shi[1], **Mark A Anastasio**[1], **Yin Huang**[1] **and Greg Gbur**[2]

[1] Department of Biomedical Engineering, Illinois Institute of Technology, Chicago, IL 60616, USA
[2] Department of Physics and Astronomy, Free University, Amsterdam, The Netherlands

E-mail: anastasio@iit.edu

Received 10 November 2003
Published 4 June 2004
Online at stacks.iop.org/PMB/49/2733
doi:10.1088/0031-9155/49/12/018

Abstract

A reconstruction theory for intensity diffraction tomography (I-DT) has been proposed that permits reconstruction of a weakly scattering object without explicit knowledge of phase information. In this work, we examine the application of I-DT, using either planar- or spherical-wave incident wavefields, for imaging three-dimensional (3D) phase objects. We develop and investigate two algorithms for reconstructing phase objects that utilize only half of the measurements that would be needed to reconstruct a complex-valued object function. Each reconstruction algorithm reconstructs the phase object by use of different sets of intensity measurements. Although the developed reconstruction algorithms are equivalent mathematically, we demonstrate that their numerical and noise propagation properties differ considerably. We implement numerically the reconstruction algorithms and present reconstructed images to demonstrate their use and to corroborate our theoretical assertions.

1. Introduction

Diffraction tomography (DT) is an imaging technique for reconstructing the complex refractive index distribution of a semi-transparent object (Wolf 1969, Devaney 1983, Mueller *et al* 1979). In DT a scalar wavefield is used to irradiate a scattering object and the scattered wavefield in the forward direction is measured on a planar detector surface. A set of tomographic measurements can be acquired by simultaneously rotating the source–detector pair around the object. An undesirable feature of DT is that it requires knowledge of both the magnitude and phase of the measured wavefields. Because of this, the success of DT imaging in optical applications has been hampered by the problem of uniquely determining the wavefield phase from knowledge of intensity measurements only.

A new theory of DT that does not require phase information was proposed recently by Gbur and Wolf (2002a, 2002b). We will refer to this new theory of DT as *intensity-DT* (I-DT). Unlike previous attempts to circumvent the lack of phase-information in DT (Devaney 1992, Maleki and Devaney 1993), the reconstruction theory of I-DT indicates that the generally complex-valued object function can be reconstructed exactly (or, more precisely, a low-pass filtered version of the object function). Similar to techniques of wavefield phase retrieval that are based on the transport-of-intensity equation (Nugent *et al* 1996, Barty *et al* 2000), I-DT requires the wavefield intensity to be measured at each view angle on two parallel detector planes that are separated by a finite distance.

The development and investigation of tomographic reconstruction techniques for imaging phase objects, i.e. scattering objects that have real-valued refractive index distributions, is currently an active research area (Nugent *et al* 1996, Barty *et al* 2000, Spanne *et al* 1999), as such objects arise in important biomedical and materials science applications. A DT approach for reconstructing phase objects from intensity measurements was proposed and investigated in Cheng and Han (2001). In that work, far-field and Born approximations and a specific scanning geometry were utilized. The recently developed I-DT reconstruction theory is more general than the method described in Cheng and Han (2001) in the sense that it does not utilize a far-field approximation and applies even when the scattering object is described by a generally complex refractive index distribution. Therefore, phase objects represent a subset of the scattering objects that can be imaged using I-DT. However, we can expect that the amount of I-DT measurement data required to perform an accurate reconstruction of a phase object will be less, in general, than the amount needed to reconstruct an arbitrary scattering object that has a complex-valued refractive index distribution.

In this work, we examine the application of I-DT, using either planar- or spherical-wave incident wavefields, for imaging two-dimensional (2D) and three-dimensional (3D) phase objects. We develop and investigate two algorithms for reconstructing phase objects that utilize only half of the measurements that would be needed to reconstruct a complex-valued object function. Each reconstruction algorithm reconstructs the phase object by use of different sets of intensity measurements. The first algorithm, referred to as a *half-scan* algorithm, requires that intensity measurements be acquired on two different measurement planes at a given view angle, but the tomographic scanning needs to cover only one half of the full angular scanning range (e.g., over the range $[0, \pi)$ in the 2D case). The second algorithm, referred to as a *single-plane* algorithm, requires that only one intensity measurement be acquired at a given view angle, but the tomographic scanning needs to cover the full angular scanning range (e.g., over the range $[0, 2\pi)$ in the 2D case). Although the reconstruction algorithms are equivalent mathematically, we demonstrate that their numerical and noise propagation properties differ considerably. We implement numerically the reconstruction algorithms and present reconstructed images to demonstrate their use and to corroborate our theoretical assertions.

2. Background

Below we review the I-DT reconstruction theory for plane-wave and spherical-wave incident wavefields as described in Gbur and Wolf (2002a, 2002b) and Gbur *et al* (2004). To facilitate the description of measurements corresponding to different tomographic view angles, we will utilize a rotated Cartesian coordinate system $\vec{r} = (x_r, y_r, z_r)$ that is related to a reference $\vec{r} = (x, y, z)$ system by

$$\begin{bmatrix} x \\ y \\ z \end{bmatrix} = \begin{bmatrix} -\sin\phi & -\cos\phi\sin\theta & \cos\phi\cos\theta \\ \cos\phi & -\sin\phi\sin\theta & \sin\phi\cos\theta \\ 0 & \cos\theta & \sin\theta \end{bmatrix} \begin{bmatrix} x_r \\ y_r \\ z_r \end{bmatrix}$$

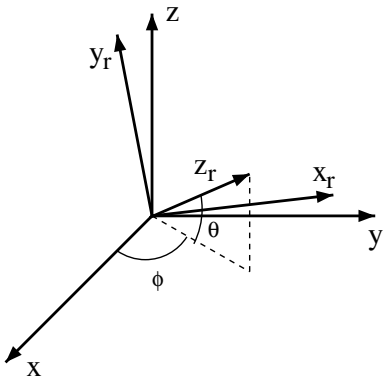

Figure 1. The (x_r, y_r, z_r) rotated coordinate system as described in section 2.

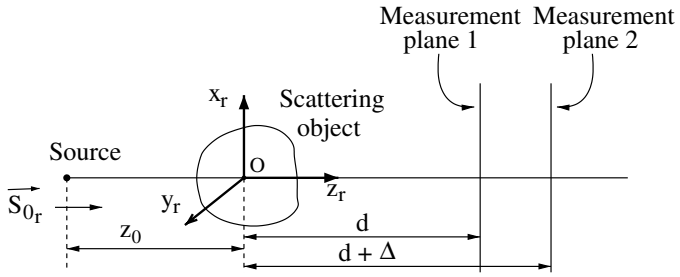

Figure 2. The tomographic scanning geometry assumes that the incident wavefield propagates along the positive z_r axis, and the detector plane(s) are parallel to the x_r–y_r plane. In the incident spherical-wave case, the source is located at a distance z_0 from the centre of the object.

where the polar (θ) and azimuthal (ϕ) angles are defined in figure 1. The unit vectors $\vec{s}_{1,r}(\phi, \theta)$, $\vec{s}_{2,r}(\phi, \theta)$ and $\vec{s}_{0,r}(\phi, \theta)$ indicate the directions of the positive x_r, y_r and z_r axes, respectively. Unless it is needed, the (ϕ, θ) dependence of the unit vectors $\vec{s}_{1,r}(\phi, \theta)$, $\vec{s}_{2,r}(\phi, \theta)$, $\vec{s}_{0,r}(\phi, \theta)$ will be suppressed in the equations below.

2.1. Plane-wave I-DT

We assume the scanning geometry illustrated in figure 2 where a monochromatic plane-wave $U_i(\vec{r}) = \exp(jk\vec{s}_{0,r} \cdot \vec{r})$, propagating in the $\vec{s}_{0,r}$ direction, is employed to probe the scattering object. Here, $k = \frac{2\pi}{\lambda}$ and λ denote the wave number and wavelength of the probing field, respectively. Two intensity measurements of the forward scattered wavefield are acquired in the x_r–y_r planes at distances $z_r = d$ and $z_r = d + \Delta$ behind the object, where $\Delta > 0$. By simultaneously rotating the incident wavefield direction and the measurement planes around the object (i.e. by varying ϕ and θ), a set of intensity measurements is acquired that can be used to reconstruct the object function $f(\vec{r})$ that is related to the complex refractive index distribution $n(\vec{r})$ as

$$f(\vec{r}) = \frac{k^2}{4\pi}[n^2(\vec{r}) - 1].$$

Below we review the basic equations that permit such a reconstruction in plane-wave I-DT.

The wavefield beyond the scatterer can be represented as

$$U(\vec{r}) = U_i(\vec{r})\mathrm{e}^{\psi(\vec{r})} \tag{1}$$

where $\psi(\vec{r})$ is the complex phase function and elastic scattering is assumed. We will let $\psi(x_r, y_r, \phi, \theta; d)$ denote $\psi(\vec{r})$ evaluated on the detector plane $z_r = d$ and define

$$\hat{\psi}(u_r, v_r, \phi, \theta; d) = \frac{1}{(2\pi)^2} \iint_{\mathbb{R}^2} \mathrm{d}x_r \, \mathrm{d}y_r \psi(x_r, y_r, \phi, \theta; d) \, \mathrm{e}^{-j(u_r x_r + v_r y_r)} \tag{2}$$

and

$$\hat{F}(\vec{K}) = \frac{1}{(2\pi)^3} \int_{\mathbb{R}^3} \mathrm{d}\vec{r} \, f(\vec{r}) \, \mathrm{e}^{-j\vec{K}\cdot\vec{r}} \tag{3}$$

as the 2D and 3D Fourier transforms of $\psi(x_r, y_r, \phi, \theta; d)$ and $f(\vec{r})$, respectively. Under the first Rytov approximation, $\hat{\psi}(u_r, v_r, \phi, \theta; d)$ and $\hat{F}(\vec{K})$ are related by the Fourier diffraction projection (FDP) theorem as (Wolf 1969, Devaney 1983, Mueller *et al* 1979)

$$\hat{\psi}(u_r, v_r, \phi, \theta; d) = \frac{(2\pi)^2 j}{w_r} \underbrace{\hat{F}(u_r \vec{s}_{1,r} + v_r \vec{s}_{2,r} + (w_r - k)\vec{s}_{0,r})}_{\hat{F}[u_r, v_r, \phi, \theta]} \, \mathrm{e}^{j(w_r - k)d} \tag{4}$$

where

$$w_r = \sqrt{k^2 - u_r^2 - v_r^2}$$

and

$$\hat{F}[u_r, v_r, \phi, \theta] \equiv \hat{F}(u_r \vec{s}_{1,r} + v_r \vec{s}_{2,r} + (w_r - k)\vec{s}_{0,r}). \tag{5}$$

We will assume that $u_r^2 + v_r^2 \leqslant k^2$ and therefore w_r will be a real-valued quantity. This reflects that the evanescent modes of $U(\vec{r})$ will not, in general, be measurable in practice.

An intensity data function $D_I(x_r, y_r, \phi, \theta; d)$ can be defined as

$$D_I(x_r, y_r, \phi, \theta; d) \equiv \ln[I(x_r, y_r, \phi, \theta; d)] = \psi(x_r, y_r, \phi, \theta; d) + \psi^*(x_r, y_r, \phi, \theta; d) \tag{6}$$

where $I(x_r, y_r, \phi, \theta; d) = \mathrm{e}^{\psi(x_r, y_r, \phi, \theta; d) + \psi^*(x_r, y_r, \phi, \theta; d)}$ is the wavefield intensity on the detector plane $z_r = d$ and ψ^* denotes the complex conjugate of ψ. The 2D Fourier transform of $D_I(x_r, y_r, \phi, \theta; d)$ is related to the 3D Fourier transform of $f(\vec{r})$ as

$$\hat{D}_I(u_r, v_r, \phi, \theta; d) = \frac{j(2\pi)^2}{w_r} [\hat{F}[u_r, v_r, \phi, \theta] \, \mathrm{e}^{j(w_r - k)d} - \hat{F}^*[-u_r, -v_r, \phi, \theta] \, \mathrm{e}^{-j(w_r - k)d}]. \tag{7}$$

At each view angle the intensities $I(x_r, y_r, \phi, \theta; d)$ and $I(x_r, y_r, \phi, \theta; d + \Delta)$ are measured, so $\hat{D}_I(u_r, v_r, \phi, \theta; d)$ and $\hat{D}_I(u_r, v_r, \phi, \theta; d + \Delta)$ can be regarded as known quantities. From this knowledge, equation (7) can be employed to establish a system of two equations involving the two unknowns $\hat{F}[u_r, v_r, \phi, \theta]$ and $\hat{F}^*[-u_r, -v_r, \phi, \theta]$ that can be solved readily to obtain

$$\hat{F}[u_r, v_r, \phi, \theta] = \frac{\hat{D}_I(u_r, v_r, \phi, \theta; d) - \hat{D}_I(u_r, v_r, \phi, \theta; d + \Delta) \, \mathrm{e}^{j(w_r - k)\Delta}}{j(2\pi)^2 \, \mathrm{e}^{j(w_r - k)d} \{1 - \mathrm{e}^{2j(w_r - k)\Delta}\} / w_r} \tag{8}$$

which is the key result of (plane-wave) I-DT and can be interpreted as the I-DT version of the FDP theorem. Equation (8) indicates that the wavefield intensities measured on the two planes $z_r = d$ and $z_r = d + \Delta$ at a particular view angle can be used to determine the spatial frequency components of $f(\vec{r})$ on the shifted Ewald sphere surface $u_r \vec{s}_{1,r} + v_r \vec{s}_{2,r} + (w_r - k)\vec{s}_{0,r}$. When the incident wavefield direction and the measurement planes are simultaneously rotated to cover a 4π solid angular range, the frequency components of f that reside inside of a sphere of radius $\sqrt{2}k$ that is centred at the origin can be determined. From this Fourier data, a conventional DT reconstruction algorithm (Devaney 1982, Pan 1998, Anastasio and Pan 2000) can be employed for reconstruction of a low-pass filtered version of the object function $f(\vec{r})$. Throughout this paper, terminology such as 'reconstruction of $f(\vec{r})$'

will always be taken to mean the reconstruction of the appropriately low-pass filtered version of $f(\vec{r})$.

2.2. Spherical-wave I-DT

The reconstruction theory of I-DT has also been generalized to account for curvature in the incident wavefield (Gbur *et al* 2004). Let the probing wavefield be a monochromatic spherical-wave of the form

$$U_i(\vec{r}) = \frac{e^{jk|\vec{r}-\vec{r}_0|}}{|\vec{r}-\vec{r}_0|} \tag{9}$$

where $\vec{r}_0 = (0, 0, -z_0)$ is the location of a point source (see figure 2). As in the plane-wave case, at each view angle the intensities of the forward-scattered wavefields are measured on the detector planes $z_r = d$ and $z_r = d + \Delta$, and will be denoted by $I_{z_0}(x_r, y_r, \phi, \theta; d)$ and $I_{z_0}(x_r, y_r, \phi, \theta; d + \Delta)$, respectively. Here, note that the subscript z_0 has been added to make explicit the dependence of the measured intensities on the source location. It will be useful to define an intensity data function as

$$D_{z_0}(x_r, y_r, \phi, \theta; z_r) = \frac{1}{|\vec{r}-\vec{r}_0|} \ln\left[I_{z_0}(x_r, y_r, \phi, \theta; z_r)\right] \tag{10}$$

where $\vec{r} = (x_r, y_r, z_r)$ describes a point on the detector plane.

Through use of a FDP theorem for the fan-beam geometry (Devaney 1985), the 2D Fourier transform of $D_{z_0}(x_r, y_r, \phi, \theta; z_r)$ can be related to the 3D Fourier transform of $f(\vec{r})$ by the equation

$$\begin{aligned}\hat{D}_{z_0}(u_r, v_r, \phi, \theta; z_r) = \frac{(2\pi)^2 j}{z_0 w_{\alpha,r} \alpha^2} \{ & \hat{F}[u_r/\alpha^2, v_r/\alpha^2, \phi, \theta]\, e^{j(w_{\alpha,r}-k)z_r} \\ & - \hat{F}^*[-u_r/\alpha^2, -v_r/\alpha^2, \phi, \theta]\, e^{-j(w_{\alpha,r}-k)z_r}\}\end{aligned} \tag{11}$$

where

$$\alpha = \sqrt{\frac{z_0}{z_r + z_0}} \tag{12}$$

and

$$w_{\alpha,r} = \sqrt{k^2 - \left(\frac{u_r}{\alpha}\right)^2 - \left(\frac{v_r}{\alpha}\right)^2}. \tag{13}$$

The fan-beam FDP theorem (Devaney 1985), and consequently equation (11), assumes that both the source location $\vec{r}_0$ and observation location $\vec{r}$ are sufficiently far from the scattering object so that paraxial approximations may be used when describing the incident and scattered wavefields. Similar to the plane-wave case, one can attempt to utilize equation (11) along with the two intensity measurements obtained at a given view angle to establish a system of two equations and two unknowns that can be solved for $\hat{F}[u_r/\alpha^2, v_r/\alpha^2, \phi, \theta]$. However, it is not possible to accomplish this if the source-to-object distance z_0 is kept constant because the intensity measurements acquired on the $z_r = d$ and $z_r = d + \Delta$ planes will be related to different spatial frequency components of $f(\vec{r})$ via equation (11) (because the values of α will be distinct). To circumvent this problem, when making the intensity measurement of the second plane, the source-to-object distance z_0 can be chosen to ensure that the parameter α remains fixed. It can be shown that the measurements $I_{z_0}(x_r, y_r, \phi, \theta; z = d)$ and $I_{z_0'}(x_r, y_r, \phi, \theta; z = d + \Delta)$ where

$$z_0' = \frac{z_0(d + \Delta)}{d} \tag{14}$$

along with equations (10) and (11) can be used to establish a system of two equations and two unknowns that can be solved to obtain

$$\hat{F}[u_r/\alpha^2, v_r/\alpha^2, \phi, \theta] = \frac{\hat{D}_{z_0}(u_r, v_r, \phi, \theta; d) - \hat{D}_{z_0'}(u_r, v_r, \phi, \theta; d + \triangle)\, \mathrm{e}^{j(w_{\alpha,r}-k)\triangle} z_0'/z_0}{j(2\pi)^2\, \mathrm{e}^{j(w_{\alpha,r}-k)d}[1 - \mathrm{e}^{j2(w_{\alpha,r}-k)\triangle}]/(z_0 w_{\alpha,r}\alpha^2)}. \tag{15}$$

When the incident wavefield direction and the measurement planes are simultaneously rotated to cover a 4π solid angular range, the above procedure indicates that the frequency components residing inside of a sphere of radius $k\sqrt{1+\frac{1}{\alpha}}$ that is centred at the origin can be determined completely. From this Fourier data, a spherical-wave DT reconstruction algorithm (Devaney 1985, Lu 1985, Anastasio and Pan 2003) can be employed for reconstruction of the object function $f(\vec{r})$.

3. Half-scan and single-plane reconstruction algorithms for I-DT imaging of phase objects

Below we develop and investigate two I-DT reconstruction algorithms for reconstructing phase objects that each utilize only half of the measurements that would be needed by a conventional I-DT reconstruction algorithm for reconstruction of an arbitrary complex-valued object function.

The algorithms below exploit the fact that, because $f(\vec{r})$ is real valued for a phase object, its Fourier transform $\hat{F}(\vec{K})$ possesses the conjugate-symmetry property

$$\hat{F}(\vec{K}) = \hat{F}^*(-\vec{K}) \tag{16}$$

or, equivalently,

$$\hat{F}[u_r, v_r, \phi, \theta] = \hat{F}^*[u_r, v_r, \phi^\pi, \theta^\pi] \tag{17}$$

where

$$\phi^\pi \equiv \phi + \pi \qquad \text{and} \qquad \theta^\pi \equiv \theta + \pi.$$

Figure 3 demonstrates graphically equation (17) for the 2D case. For the spherical-wave DT case, equation (16) implies the symmetry

$$\hat{F}[u_r/\alpha^2, v_r/\alpha^2, \phi, \theta] = \hat{F}^*[u_r/\alpha^2, v_r/\alpha^2, \phi^\pi, \theta^\pi] \tag{18}$$

which reduces to equation (17) for $\alpha = 1$. In (conventional) DT imaging, Devaney (1989) recognized that equation (17) can be exploited to reconstruct a real-valued object function from measurements taken over a π angular scanning interval, and we will utilize this fact in the next section.

3.1. Half-scan I-DT for phase objects

The terminology 'half-scan' reflects that measurements acquired over only one half of the total angular scanning range (i.e. 2π steradians in the 3D case or π radians in the 2D case) are utilized. However, as in the I-DT reconstruction theory that was described in section 2, a half-scan algorithm will require the transmitted wavefield intensity to be measured on two parallel detector planes at each view angle.

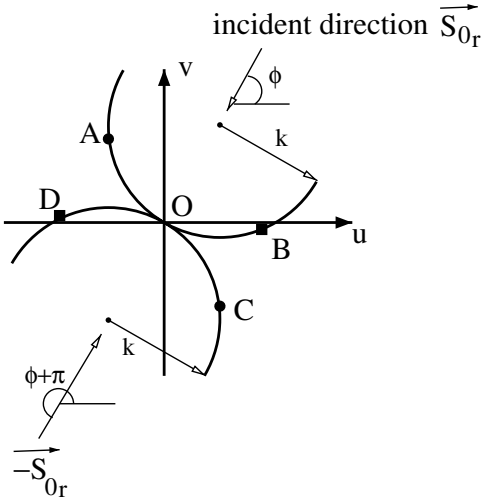

Figure 3. A 2D illustration of the conjugate-symmetry property described by equation (17). When f is real valued, the values of its Fourier transform $\hat{F}$ obtained from measurement data acquired at conjugate view angles are redundant. For example, the value of $\hat{F}$ at point A (B) is equal to the complex conjugate value of $\hat{F}$ at point C (D).

3.1.1. Half-scan reconstruction algorithm for plane-wave I-DT. A half-scan reconstruction algorithm for plane-wave I-DT can be formed as

[P-1] Use equation (8) to determine $\hat{F}[u_r, v_r, \phi, \theta]$ for (ϕ, θ) corresponding to the available view directions $\{\vec{s}_{0,r}(\phi, \theta)\}$. We assume that measurements at views $\vec{s}_{0,r}(\phi, \theta)$ or $\vec{s}_{0,r}(\phi^\pi, \theta^\pi)$ are acquired, but not both.

[P-2] Reconstruct $f(\vec{r})$ via a DT reconstruction algorithm that explicitly or implicitly utilizes equation (17) to determine the missing Fourier components of $\hat{F}$ that are conjugate to those obtained in step [P-1].

3.1.2. Half-scan reconstruction algorithm for spherical-wave I-DT. A half-scan reconstruction algorithm for spherical-wave I-DT can be formed as

[S-1] Use equation (15) to determine $\hat{F}[u_r/\alpha^2, v_r/\alpha^2, \phi, \theta]$ for (ϕ, θ) corresponding to the available view directions $\{\vec{s}_{0,r}(\phi, \theta)\}$. We assume that measurements at views $\vec{s}_{0,r}(\phi, \theta)$ or $\vec{s}_{0,r}(\phi^\pi, \theta^\pi)$ are acquired, but not both.

[S-2] Reconstruct $f(\vec{r})$ via a spherical-wave DT reconstruction algorithm that explicitly or implicitly utilizes equation (18) to determine the missing Fourier components of $\hat{F}$ that are conjugate to those obtained in step [S-1].

As an example, we consider the case where the required (two) intensity measurements are obtained at view direction $\{\vec{s}_{0,r}(\phi, \theta)\}$ for $0 \leqslant \phi < \pi, \theta = 0$. This corresponds to an experimentally feasible tomographic scanning geometry in which the incident wavefield direction $\vec{s}_{0,r}(\phi, \theta)$ and x_r-y_r detector planes at $z_r = d$ and $z_r = d + \Delta$ are rotated simultaneously through a π angular range about the z-axis. According to equations (8) or (15), the data acquired in this scanning geometry will not permit for the determination of all components of $\hat{F}$ inside the sphere of radius $k\sqrt{1 + \frac{1}{\alpha}}$, but the determined values of $\hat{F}$ can be employed for the reconstruction of a certain low-pass filtered $f(\vec{r})$. In the appendix,

we show that a 3D filtered backpropagation algorithm (Devaney 1982) can reconstruct an estimate of $f(\vec{r})$ from knowledge of $\hat{F}[u_r/\alpha^2, v_r/\alpha^2, \phi, 0]$ for $\phi \in [0, \pi)$.

3.2. Single-plane I-DT for phase objects

The necessity of the half-scan reconstruction algorithms to acquire two intensity measurements on different detector planes at each view angle is, in general, undesirable because it necessitates complications in the scanning motion that can introduce errors into the measurement data and/or increase the time needed to perform the imaging scan. In this section we develop single-plane reconstruction algorithms, where the terminology 'single-plane' reflects that only one intensity measurement at each tomographic view angle is utilized. The single-plane reconstruction algorithms assume that the object-to-detector distance is fixed, and the scanning motion corresponds to that of a conventional (full-angular scan) tomographic experiment.

3.2.1. Single-plane reconstruction algorithm for plane-wave I-DT. The plane-wave I-DT version of the FDP theorem given in equation (8) was derived by solving a system of two equations that involved the measured intensities on two different planes at a given view angle as the known quantities. We must now modify this procedure because we have only one intensity measurement at each view that is acquired in the plane $z_r = d$. From the wavefield intensity measured in the $z_r = d$ plane with orientation $\vec{s}_{0,r}(\phi, \theta)$, as before, we can obtain equation (7). To obtain a second linearly independent equation that involves the same unknowns as equation (7), consider the intensity measurement in the $z_r = d$ plane with orientation $\vec{s}_{0,r}(\phi^\pi, \theta^\pi)$. According to equation (7) we find that

$$\hat{D}_I(u_r, v_r, \phi^\pi, \theta^\pi; d) = \frac{j(2\pi)^2}{w_r}\{\hat{F}[u_r, v_r, \phi^\pi, \theta^\pi]\, \mathrm{e}^{j(w_r - k)d} - \hat{F}^*[-u_r, -v_r, \phi^\pi, \theta^\pi]\, \mathrm{e}^{-j(w_r - k)d}\}. \tag{19}$$

By taking the complex conjugate of equation (19) and utilizing equation (17), we can form an equation that involves the same unknowns as in equation (7). These two linearly independent equations can be solved to obtain

$$\hat{F}[u_r, v_r, \phi, \theta] = \frac{\hat{D}_I(u_r, v_r, \phi, \theta; d) + [\hat{D}_I(u_r, v_r, \phi^\pi, \theta^\pi; d)]^*\, \mathrm{e}^{-j2(w_r - k)d}}{j(2\pi)^2\, \mathrm{e}^{j(w_r - k)d}(1 - \mathrm{e}^{-j4(w_r - k)d})/w_r} \tag{20}$$

which represents an FDP relationship for single-plane I-DT imaging of phase-objects. Equation (20) is similar in structure to equation (8) but contains important differences that will be discussed in sections 3.3 and 3.4. The use of equation (20) for determination of $\hat{F}[u_r, v_r, \phi, \theta]$ coupled with a conventional DT reconstruction algorithm for obtaining $f(\vec{r})$ will be referred to as a *single-plane reconstruction algorithm for plane-wave I-DT*.

3.2.2. Single-plane reconstruction algorithm for spherical-wave I-DT. In the same way that equation (20) was derived, for the spherical-wave case we can obtain

$$\hat{F}[u_r/\alpha^2, v_r/\alpha^2, \phi, \theta] = \frac{\hat{D}_{z_0}(u_r, v_r, \phi, \theta; d) + \left[\hat{D}_{z_0}(u_r, v_r, \phi^\pi, \theta^\pi; d)\right]^*\, \mathrm{e}^{-j2(w_{\alpha,r} - k)d}}{j(2\pi)^2\, \mathrm{e}^{j(w_{\alpha,r} - k)d}(1 - \mathrm{e}^{-j4(w_{\alpha,r} - k)d})/(z_0 w_{\alpha,r}\alpha^2)} \tag{21}$$

where $\hat{D}_{z_0}(u_r, v_r, \phi, \theta; d)$ is defined in equation (11). Recall that in the half-scan reconstruction algorithm for spherical-wave I-DT, as formulated in section 3.1, each of the two required intensity measurements at each view angle had to correspond to distinct (and specified) values of the source location in order to keep α fixed (which was needed to establish a system of two equations with two unknowns). Equation (21) indicates that this experimental

complication is not needed in the single-plane reconstruction method because a single intensity measurement acquired at each view angle provides information that is sufficient to specify $\hat{F}$ (and hence f via a DT reconstruction algorithm). The use of equation (21) for determination of $\hat{F}[u_r/\alpha^2, v_r/\alpha^2, \phi, \theta]$ coupled with a spherical-wave DT reconstruction algorithm for obtaining $f(\vec{r})$ will be referred to as a *single-plane reconstruction algorithm for spherical-wave I-DT*.

3.3. Resolution limitations in half-scan and single-plane I-DT

Equations (8) and (20), which underlie the half-scan and single-plane reconstruction algorithms, respectively, are equivalent mathematically in the sense that, up to a set of measure zero (Wheeden and Zygmund 1977), they can both recover the same components of $\hat{F}$ from consistent (i.e. error-free) measurement data. However, equations (8) and (20) contain singularities and therefore, in practice, can be used only to estimate components of $\hat{F}$ that do not correspond to or are not near the singular points. As discussed below, the locations of singularities in equations (8) and (20) are generally different. Consequently, the estimable components of $\hat{F}$, and accordingly the reconstructed image resolutions and noise properties, will be different in half-scan and single-plane I-DT. For simplicity, we will consider here only the plane-wave case. The results that follow can be extended readily to the spherical-wave case.

3.3.1. Half-scan I-DT. As discussed in Gbur and Wolf (2002b), equation (8) becomes singular when

$$2\triangle\big(k - \sqrt{k^2 - u_r^2 - v_r^2}\big) = 2n\pi \tag{22}$$

where n is an integer. Therefore the components of $\hat{F}[u_r, v_r, \phi, \theta]$ that satisfy equation (22) cannot be determined via equation (8). Moreover, when the measured intensities contain noise, the magnitude of this noise will be amplified greatly in estimates of $\hat{F}[u_r, v_r, \phi, \theta]$ for (u_r, v_r) near a singular point (see section 3.4 below). To avoid regions of Fourier space that contain singular points, one can estimate $\hat{F}[u_r, v_r, \phi, \theta]$ at frequency components $(u_r, v_r) \neq (0, 0)$ that satisfy

$$2\triangle\big(k - \sqrt{k^2 - u_r^2 - v_r^2}\big) < 2\pi. \tag{23}$$

If

$$\hat{F}[u_r, v_r, \phi, \theta] \approx 0 \qquad \text{for } |u_r| > u_{\max} \qquad \text{and} \qquad |v_r| > v_{\max}$$

then, when $k^2 \gg u_{\max}^2 + v_{\max}^2$, equation (23) simplifies to

$$u_r^2 + v_r^2 < 2\pi k/\triangle. \tag{24}$$

Equations (23) or (24) restrict the the region of Fourier space over which $\hat{F}$ can be determined, thereby indicating how the spatial-frequency content (i.e. spatial resolution) of the reconstructed f is limited in half-scan I-DT.

3.3.2. Single-plane I-DT. On the other hand, in the single-plane I-DT algorithm, the denominator of equation (20) will be zero when

$$4d\big(k - \sqrt{k^2 - u_r^2 - v_r^2}\big) = 2n\pi. \tag{25}$$

To avoid regions of Fourier space that contain singular points, one can estimate $\hat{F}[u_r, v_r, \phi, \theta]$ at frequency components $(u_r, v_r) \neq (0, 0)$ that satisfy

$$4d\left(k - \sqrt{k^2 - u_r^2 - v_r^2}\right) < 2\pi \tag{26}$$

or, when $k^2 \gg u_{\max}^2 + v_{\max}^2$,

$$u_r^2 + v_r^2 < \pi k/d. \tag{27}$$

Equation (26) or (27) restrict the the region of Fourier space over which $\hat{F}$ can be determined, thereby indicating how the spatial-frequency content (i.e. spatial resolution) of the reconstructed f is limited in single-plane I-DT.

The above observations have implications on the choice of scanning geometries that are best suited for use with half-scan and single-plane I-DT. According to equation (27), for a given k, the spatial resolution of images reconstructed by use of the single-plane algorithm can be increased by use of a scanning system with a small object-to-detector distance d. Of course, the detector plane cannot intersect the support of the scattering object, so the radius of the scattering object establishes a minimum realizable value for d. According to equation (24), the resolution of images reconstructed by use of the half-scan algorithm is limited only by k and the detector plane spacing Δ, and is independent of d. To maximize the image resolution, one can therefore utilize a small value for Δ, but, as discussed below, this strategy can significantly amplify the noise levels of the low-frequency components of the reconstructed f (Gbur and Wolf 2002c). According to equations (24) and (27), the sets of estimable components of $\hat{F}$ in the half-scan and single-plane methods will coincide when $\Delta = 2d$. Otherwise stated, the locations of the singularities corresponding to $n = 1$ in equations (23) and (26) (that we need to avoid) will coincide when $\Delta = 2d$. When $\Delta < 2d$ the distance from the origin of the object's 3D Fourier space to the location of the singular points will be larger in the half-scan method than in the single-plane method. As such, the half-scan method will be capable of recovering more high-frequency components of $\hat{F}$ than can the single-plane method. The converse is true when $\Delta > 2d$.

The origin of the singularities in equations (8) and (20) lies in the periodicity of the Fourier transform of the intensity data function (equation (7)) in the z_r direction. In the half-scan configuration, when the two detector planes are spaced by a distance Δ such that equation (22) is satisfied, the equations that relate $\hat{D}_I$ on the two measurement planes to the object function are linearly dependent and cannot be used to determine $\hat{F}$. Similarly, in the single-plane configuration, when the measurement plane distance d satisfies equation (25), the equations that relate $\hat{D}_I$ at view angles (θ, ϕ) and (θ^π, ϕ^π) to the object function are linearly dependent and cannot be used to determine $\hat{F}$.

3.4. Noise amplification in half-scan and single-plane I-DT

In addition to imposing a practical limit to the image resolution, the singularities in the denominators of equations (8) and (20) can influence dramatically the statistical variance of the reconstructed images. Again, we will consider here the plane-wave case, but the results below can be generalized readily to the spherical-wave case.

3.4.1. Half-scan I-DT. We assume now that the intensity measurements are corrupted by some source of stochastic noise and treat the intensity data functions $\boldsymbol{D_I}(x_r, y_r, \phi, \theta; d)$ and $\boldsymbol{D_I}(x_r, y_r, \phi, \theta; d + \Delta)$ as random variables. (Here and in the following, a boldface font will denote a random variable.) If we define

$$\boldsymbol{D_{hs}}(u_r, v_r, \phi, \theta) \equiv \hat{\boldsymbol{D}}_{\boldsymbol{I}}(u_r, v_r, \phi, \theta; d) - \hat{\boldsymbol{D}}_{\boldsymbol{I}}(u_r, v_r, \phi, \theta; d + \triangle)\, \mathrm{e}^{j(w_r - k)\triangle} \tag{28}$$

then by use of equation (8) one finds readily that

$$\mathrm{Var}\{\hat{\boldsymbol{F}}^{hs}[u_r, v_r, \phi, \theta]\} = \frac{w_r^2}{(2\pi)^4} \frac{\mathrm{Var}\{\boldsymbol{D}_{hs}(u_r, v_r, \phi, \theta)\}}{2\,[1 - \cos(2(w_r - k)\Delta)]} \tag{29}$$

where $\mathrm{Var}\{\cdot\}$ denotes the variance of a random variable and the superscript 'hs' denotes that $\hat{\boldsymbol{F}}^{hs}[u_r, v_r, \phi, \theta]$ is obtained by use of the half-scan I-DT algorithm (i.e. equation (8)). Equation (29) describes how $\mathrm{Var}\{\hat{\boldsymbol{F}}^{hs}[u_r, v_r, \phi, \theta]\}$ depends on $\mathrm{Var}\{\boldsymbol{D}_{hs}(u_r, v_r, \phi, \theta)\}$ (determined from the measured data), wave number k and the detector spacing Δ. Note that, for any realistic noise model, $\mathrm{Var}\{\boldsymbol{D}_{hs}(u_r, v_r, \phi, \theta)\}$ remains finite for all u_r and v_r. Therefore $\mathrm{Var}\{\hat{\boldsymbol{F}}^{hs}[u_r, v_r, \phi, \theta]\}$ becomes unbounded as $(u_r, v_r) \to (0, 0)$ and as $(u_r, v_r) \to (u_{hs}, v_{hs})$, where (u_{hs}, v_{hs}) is a singular point that satisfies equation (22) for $n = 1$.

3.4.2. Single-plane I-DT. If we define

$$\boldsymbol{D}_{sp}(u_r, v_r, \phi, \theta) \equiv \hat{\boldsymbol{D}}_I(u_r, v_r, \phi, \theta; d) + [\hat{\boldsymbol{D}}_I(u_r, v_r, \phi^{\pi}, \theta^{\pi}; d)]^* \, \mathrm{e}^{-j2(w_r - k)d} \tag{30}$$

then by use of equation (20) one can show that

$$\mathrm{Var}\{\hat{\boldsymbol{F}}^{sp}[u_r, v_r, \phi, \theta]\} = \frac{w_r^2}{(2\pi)^4} \frac{\mathrm{Var}\{\boldsymbol{D}_{sp}(u_r, v_r, \phi, \theta)\}}{2\,[1 - \cos(4(w_r - k)d)]} \tag{31}$$

where the superscript 'sp' denotes that $\hat{\boldsymbol{F}}^{sp}[u_r, v_r, \phi, \theta]$ is obtained by use of the single-plane I-DT method (i.e. equation (20)). We see that $\mathrm{Var}\{\hat{\boldsymbol{F}}^{sp}[u_r, v_r, \phi, \theta]\}$ becomes unbounded as $(u_r, v_r) \to (0, 0)$ and as $(u_r, v_r) \to (u_{sp}, v_{sp})$, where (u_{sp}, v_{sp}) is a singular point that satisfies equation (25) for $n = 1$.

The above discussions indicate that the variance in the estimates $\hat{\boldsymbol{F}}^{sp}[u_r, v_r, \phi, \theta]$ and $\hat{\boldsymbol{F}}^{hs}[u_r, v_r, \phi, \theta]$ becomes exceedingly large for (u_r, v_r) near a singular point. The noise amplification problem associated with the (non-zero) singular points located at $\{(u_{sp}, v_{sp})\}$ or $\{(u_{hs}, v_{hs})\}$ can be circumvented readily by restricting the range of (u_r, v_r) values that $\hat{F}$ is estimated over. For example, equations (24) and (27) can be replaced by the more restrictive conditions

$$u_r^2 + v_r^2 < 2\pi k/\Delta - \epsilon_1, \tag{32}$$

and

$$u_r^2 + v_r^2 < \pi k/d - \epsilon_2, \tag{33}$$

respectively, where $\epsilon_1, \epsilon_2 > 0$ can be regarded as real-valued regularization parameters (that can be chosen according to some rule that makes use of knowledge of the noise properties). In effect, this regularization strategy directly sacrifices the spatial-frequency content of the reconstructed f in exchange for stability.

The noise amplification problem associated with the singular point at the origin must be handled differently. Without knowledge of $\hat{F}[u, v, \phi, \theta]$ for (u, v) near the origin, the reconstructed image will generally contain significant distortions and inaccuracies. Accordingly, we cannot simply trade the spatial-frequency content of f for stability by setting $\hat{F}[u, v, \phi, \theta] = 0$ for (u, v) near the origin. However, the effects of noise amplification can be mitigated by use of certain scanning geometries that employ sufficiently large values for Δ (for the half-scan method) and d (for the single-plane method). To understand this, we can consult the variance expressions in equations (29) and (31). The key observation is that, for (u, v) near $(0, 0)$, the values of the denominators in equations (29) and (31) increase as the values of Δ and d increase, respectively, thereby reducing $\mathrm{Var}\{\hat{\boldsymbol{F}}^{sp}[u_r, v_r, \phi, \theta]\}$ and $\mathrm{Var}\{\hat{\boldsymbol{F}}^{hs}[u_r, v_r, \phi, \theta]\}$, respectively. In the results section, we demonstrate numerically the regularizing effect that suitable choices for Δ and d can have in half-scan and single-plane

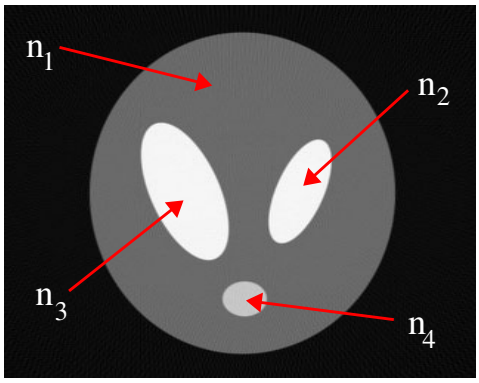

Figure 4. An image of the mathematical phantom.

I-DT. As usual, the price to pay for this regularization is decreased spatial-resolution of the reconstructed f. Recall that, according to the conclusions of section 3.3, the spatial-frequency content of the reconstructed images in half-scan and single-plane I-DT varies inversely with Δ and d, respectively.

4. Simulation studies

We performed simulation studies to corroborate our theoretical assertions and to investigate the numerical properties of the half-scan and single-plane reconstruction algorithms.

4.1. Phantom and simulation data

A 2D mathematical phantom that contained four uniform ellipses, shown in figure 4, was utilized in our simulation studies. The length of the long axis of ellipse #1 (the largest ellipse) was 0.55 (arbitrary units). Two versions of the phantom were constructed. The first phantom contained only real-valued refractive index values and will be referred to as the 'phase object', for which the refractive index values n_1, n_2, n_3 and n_4 are 1.001, 1.0025, 1.0025 and 1.002, respectively. The second phantom had complex refractive index values for two of the ellipses ($n_2 = n_3 = 1.0025 + j0.005$) and will be referred to as the 'complex object'. As described later, the complex object will be employed to investigate how the reconstruction algorithms respond to the violation of the assumption that $f(\vec{r})$ is real valued (i.e. equation (16)).

The 2D scanning configuration shown in figure 5 was employed, which is described by the coordinate system in figure 1 with $\theta = 0$. The probing wavefield was a plane-wave travelling along the positive z_r-axis (with $\lambda = 1 \times 10^{-6}$ or $\lambda = 1 \times 10^{-3}$) and the linear detector array had a length of 3.072 and contained 1024 elements (therefore the detector sampling interval was $\Delta x_r = 0.003$). For the single-plane method, three different object-to-detector distances $d = 0.4, 0.9, 1.8$ were used. For the half-scan method, six detector plane spacing intervals $\Delta = 0.005, 0.01, 0.1, 0.3, 0.6, 1.2$ were used in combination with one of the d values listed above.

The complex phases $\psi(x_r, \phi; d)$ on the detector arrays were calculated analytically by use of equation (4), and the intensity functions were formed as $I(x_r, \phi; d) = \mathrm{e}^{\psi(x_r,\phi;d)+\psi^*(x_r,\phi;d)}$. Note that the phantom objects were, by construction, weakly scattering objects. The deleterious effects of strong scattering in linearized DT are well known (Slaney *et al* 1984, Chen and Stamnes 1998) and are not investigated in this work. In the experiments for the

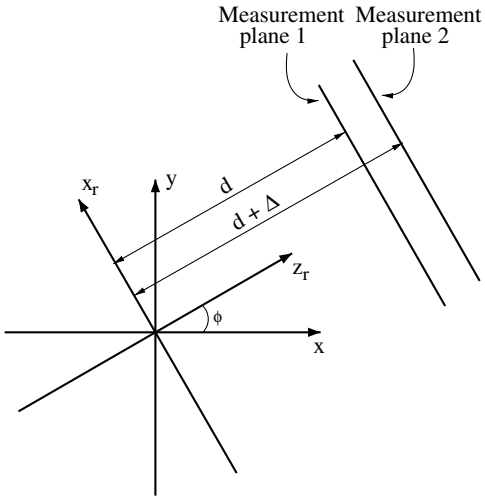

Figure 5. A schematic of the 2D scanning geometry that was employed in the numerical experiments.

single-plane method, $I(x_r, \phi; d)$ was calculated at 360 evenly erspaced view angles over the interval $[0, 2\pi)$. In the experiments for the half-scan and conventional I-DT methods, $I(x_r, \phi; d)$ and $I(x_r, \phi; d + \Delta)$ were calculated at 180 evenly spaced view angles over the interval $[0, \pi)$ and 360 evenly spaced view angles over the interval $[0, 2\pi)$, respectively.

4.2. Noise model

To investigate the noise propagation properties of the algorithms, the intensity data were treated as realizations of an uncorrelated Gaussian stochastic process that was characterized by its mean μ and standard deviation σ. When generating the noisy data, μ was set equal to the noiseless value of $I(x_r, \phi; z_r)$ at a given detector location and σ was chosen to satisfy $\frac{\sigma}{\mu} = 0.5\%$ or $\frac{\sigma}{\mu} = 1.0\%$.

4.3. Reconstruction procedure

Using the single-plane and half-scan algorithms, images were reconstructed from the noiseless and noisy measurement data. For the single-plane algorithm, we formed $D_I(x_r, \phi; d) = \ln[I(x_r, \phi; d)]$ and used equation (20) (with the explicit v_r dependence removed and $w_r \equiv \sqrt{k^2 - u_r^2}$) to obtain $\hat{F}[u_r, \phi]$. For the half-scan algorithm, $D_I(x_r, \phi; d) = \ln[I(x_r, \phi; d)]$ and $D_I(x_r, \phi; d + \Delta) = \ln[I(x_r, \phi; d + \Delta)]$ were calculated and used in equation (8) (with the explicit v_r dependence removed and $w_r \equiv \sqrt{k^2 - u_r^2}$) to obtain $\hat{F}[u_r, \phi]$. For each ϕ, $\hat{F}[u_r, \phi]$ was determined at 1024 evenly spaced samples over the interval $\left[-\frac{\pi}{\Delta x_r}, \frac{\pi}{\Delta x_r}\right]$, where $\Delta x_r = 0.003$. The phantom objects were quasi-bandlimited and satisfied $|\hat{F}[u_r, \phi]| \approx 0$ for $|u_r| > \frac{\pi}{\Delta x_r}$. In both the single-plane and half-scan algorithms, from the determined $\hat{F}[u_r, \phi]$, $f(x, z)$ was reconstructed by use of a discretized version of the filtered backpropagation formula

$$f(x, y) = \mathrm{Re}\left\{\int_0^{\pi} \mathrm{d}\phi \int_{u_r^2 \leqslant k^2} \mathrm{d}u_r \frac{k|u_r|}{w_r} \hat{F}[u_r, \phi]\, \mathrm{e}^{j(u_r x_r + (w_r - k)z_r)}\right\} \tag{34}$$

(a) (b) (c)

Figure 6. Images of the phase object reconstructed from noiseless data by use of the (a) single-plane, (b) half-scan and (c) conventional I-DT reconstruction algorithms. The scanning geometries corresponded to the values $\lambda = 1 \times 10^{-6}$, $d = 1.8$ and $\Delta = 0.1$ (arbitrary units).

(a) (b) (c)

Figure 7. Images of the phase object reconstructed from noiseless data by use of the (a) single-plane, (b) half-scan and (c) conventional I-DT reconstruction algorithms. The scanning geometries corresponded to the values $\lambda = 1 \times 10^{-3}$, $d = 0.4$ and $\Delta = 0.05$.

where $x = -x_r \sin\phi + z_r \cos\phi$ and $y = x_r \cos\phi + z_r \sin\phi$, which is the 2D equivalent of equation (A.4) with $\alpha = 1$. For comparison, images were also reconstructed by use of equation (8) to estimate $\hat{F}[u_r, \phi]$ for $\phi \in [0, 2\pi)$ coupled with the conventional 2D-filtered backpropagation algorithm (Devaney 1982) that backpropagates over a 2π angular range and does not assume the symmetry given in equation (17). We will refer to this algorithm, which can reconstruct a generally complex-valued object function, as the 'conventional' I-DT reconstruction algorithm. In all cases, the reconstructed images were represented by a 201×201 matrix with pixel dimensions $\Delta x = \Delta z = 0.003$.

5. Reconstructed images and discussion

5.1. Reconstructed images of phase object

Figures 6 and 7 contain images of the phase object that were obtained by use of the single-plane (figures 6(a) and 7(a)), half-scan (figures 6(b) and 7(b)) and conventional I-DT reconstruction algorithm (figures 6(c) and 7(c)) from noiseless data corresponding to two scanning geometries having different parameters λ, d and Δ. Figure 6 shows the images for the scanning geometry $\lambda = 1 \times 10^{-6}$, $d = 1.8$ and $\Delta = 0.1$ (recall that Δ is relevant to the half-scan and conventional methods only). In this case, all of the reconstruction methods produced images that were accurate representations of the true phantom shown in figure 4. This is explained by the fact that, for the given values of λ, d and Δ, $\hat{F}[u_r, \phi]$ can be estimated for all non-zero $u_r \in \left[-\frac{\pi}{\Delta x_r}, \frac{\pi}{\Delta x_r}\right]$. This is because the locations of the singularities described by equation (27)

(a) (b) (c)

Figure 8. Images of the phase object reconstructed from noisy data with $\frac{\sigma}{\mu} = 0.5\%$ by use of the (a) single-plane, (b) half-scan and (c) conventional I-DT reconstruction algorithms. The scanning geometries corresponded to the values $\lambda = 1 \times 10^{-6}$, $d = 1.8$ and $\Delta = 0.3$.

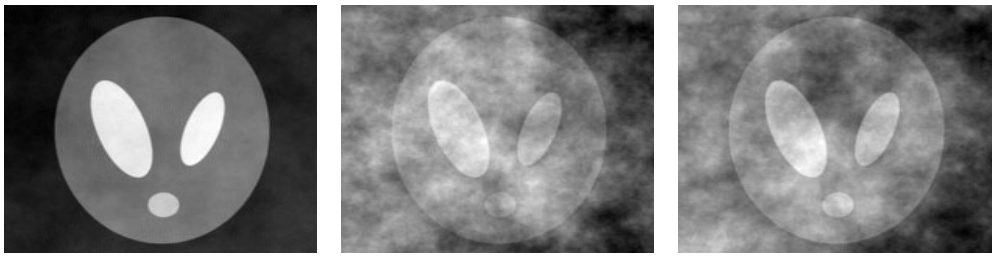

(a) (b) (c)

Figure 9. Images of the phase object reconstructed from noisy data with $\frac{\sigma}{\mu} = 1.0\%$ by use of the (a) single-plane, (b) half-scan and (c) conventional I-DT reconstruction algorithms. The scanning geometries corresponded to the values $\lambda = 1 \times 10^{-6}$, $d = 1.8$ and $\Delta = 0.3$.

($\sqrt{\frac{\pi k}{d}}$ for the single-plane method) and equation (24) ($\sqrt{\frac{2\pi k}{\Delta}}$ for the half-scan and conventional methods) (with $v_r = 0$ in this 2D example) lie outside the interval $\left[-\frac{\pi}{\Delta x_r}, \frac{\pi}{\Delta x_r}\right]$. Figure 7 shows the images for the scanning geometry $\lambda = 1 \times 10^{-3}, d = 0.4$ and $\Delta = 0.01$ (it is to be noted that the wavelength is much larger in this example). We find now that the image reconstructed by use of the single-plane method (figure 7(a)) is no longer an accurate approximation of $f(x, z)$. This occurs because $\hat{F}[u_r, \phi]$ is estimated only for all non-zero $u_r \in \left(-\sqrt{\frac{\pi k}{d}}, \sqrt{\frac{\pi k}{d}}\right)$, where $\sqrt{\frac{\pi k}{d}} < \frac{\pi}{\Delta x_r}$, because the location of the singularity at $u_r = \sqrt{\frac{\pi k}{d}}$ now resides inside the quasi-bandwidth region $\left[-\frac{\pi}{\Delta x_r}, \frac{\pi}{\Delta x_r}\right]$. As a result, $\hat{F}[u_r, \phi]$ is not determined for $u_r \in \left[-\frac{\pi}{\Delta x_r}, -\sqrt{\frac{\pi k}{d}}\right) \bigcup \left(\sqrt{\frac{\pi k}{d}}, \frac{\pi}{\Delta x_r}\right]$ and the reconstructed image is a blurred approximation of $f(x, y)$. The images reconstructed by use of the half-scan and conventional algorithms shown in figures 7(b) and (c), respectively, appear virtually identical to those shown in figures 6(b) and (c), respectively, reflecting that the singularity located at $\sqrt{\frac{2\pi k}{\Delta}}$ remains outside the quasi-bandwidth interval $\left[-\frac{\pi}{\Delta x_r}, \frac{\pi}{\Delta x_r}\right]$ for this scanning geometry.

Figures 8–11 display images of the phase object that were reconstructed from the noisy data corresponding to scanning geometries having different parameters λ, d and Δ. Figures 8 and 9 contain images corresponding to scanning geometries with $\lambda = 1 \times 10^{-6}, d = 1.8$ and $\Delta = 0.3$, reconstructed from noisy data with $\frac{\sigma}{\mu} = 0.5\%$ and $\frac{\sigma}{\mu} = 1.0\%$, respectively. The images reconstructed by use of the single-plane algorithm (figures 8(a) and 9(a)) appear virtually unaffected by the data noise unlike the images reconstructed by use of the half-scan algorithm (figures 8(b) and 9(b)) that are significantly corrupted by noise. It is also apparent

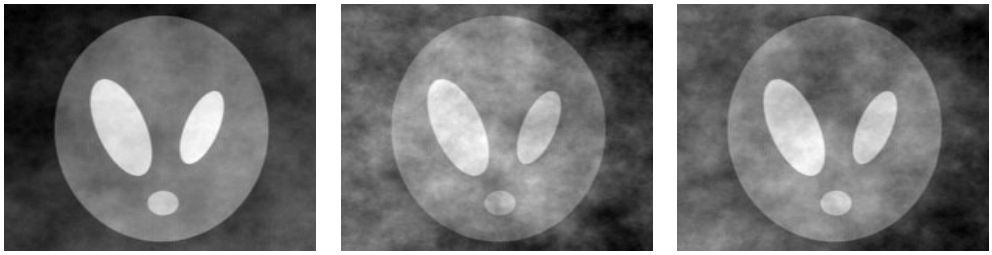

(a) (b) (c)

Figure 10. Images of the phase object reconstructed from noisy data with $\frac{\sigma}{\mu} = 1.0\%$ by use of the (a) single-plane, (b) half-scan and (c) conventional I-DT reconstruction algorithms. The scanning geometries corresponded to the values $\lambda = 1 \times 10^{-6}$, $d = 0.9$ and $\Delta = 0.6$.

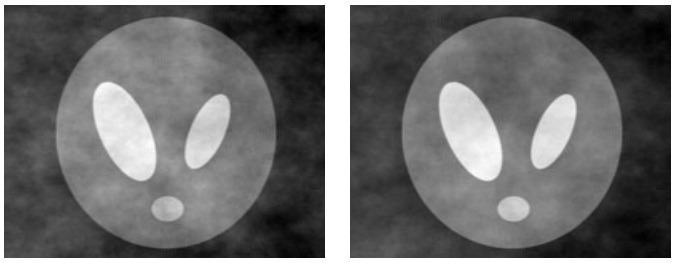

(a) (b)

Figure 11. Images of the phase object reconstructed from noisy data with $\frac{\sigma}{\mu} = 1.0\%$ by use of the (a) half-scan and (b) conventional I-DT reconstruction algorithms. The scanning geometries corresponded to the values $\lambda = 1 \times 10^{-6}$, $d = 0.9$ and $\Delta = 1.2$.

that the noise in figures 8(b) and 9(b) resides primarily in the low-frequency components of the reconstructed images. These observations are consistent with our noise analysis in section 3.4. Because $\Delta \ll 2d$, equations (29) and (31) predict that the variance of the low-frequency components of $f(x, y)$ will be much more amplified in the half-scan algorithm than in the single-plane algorithm. The images reconstructed by use of the conventional I-DT algorithm are shown in figures 8(c) and 9(c). The texture of the noise appears similar to that of the images reconstructed by use of the half-scan algorithm, but the magnitude of the noise is diminished because twice as many measurement data are utilized for reconstruction of $f(x, y)$, which serves to eliminate certain components of the data noise.

Figures 10 and 11, which display images of the phase object that were reconstructed from noisy data with $\frac{\sigma}{\mu} = 1.0\%$ and $\lambda = 1 \times 10^{-6}$, demonstrate further how the choices of d and Δ can influence the noise properties of the images reconstructed by use of the single-plane and half-scan algorithms, respectively. The images shown in figure 10 correspond to scanning geometries with $d = 0.9$ and $\Delta = 0.6$, which are one-half and twice the values for d and Δ, respectively, that were employed in figure 9. The magnitude of the noise in the image reconstructed by use of the single-plane algorithm in figure 10(a) is larger than the corresponding image in figure 9(a), which shows, consistent with equation (31), that the magnitude of the noise components in the low-frequency components of f will increase as d decreases. Conversely, the magnitude of the noise in the image reconstructed by use of the half-scan algorithm in figure 10(b) is less than in figure 9(b) because the value of Δ that corresponds to figure 10(b) is larger. Although, in this example, the value of d cannot

(a) (b) (c)

Figure 12. Images of the complex object reconstructed from noiseless data by use of the (a) single-plane, (b) half-scan and (c) conventional I-DT reconstruction algorithms. The scanning geometries corresponded to the values $\lambda = 1 \times 10^{-3}$, $d = 1.8$ and $\Delta = 0.005$.

(a) (b) (c)

Figure 13. Images of the complex object reconstructed from noiseless data by use of the (a) single-plane, (b) half-scan and (c) conventional I-DT reconstruction algorithms. The scanning geometries corresponded to the values $\lambda = 1 \times 10^{-6}$, $d = 1.8$ and $\Delta = 0.005$.

be substantially reduced without having the detector line intersect the object function, we are free to make Δ larger to investigate its impact on the noise properties of the half-scan algorithm. In figure 11 the detector plane spacing corresponds to $\Delta = 1.2$. Figure 11(a) shows the image reconstructed using the half-scan algorithm, while figure 11(b) shows the image reconstructed by use of the conventional I-DT algorithm. Consistent with our noise analysis, these figures demonstrate that the magnitude of the noise in the reconstructed images decreases as Δ increases.

5.2. Reconstructed images of complex object

Figures 12 and 13 display images of the complex object that were reconstructed from noiseless data corresponding to scanning geometries with $d = 1.8$, $\Delta = 0.005$ with $\lambda = 1 \times 10^{-3}$ and $\lambda = 1 \times 10^{-6}$, respectively. As before, the sub-figures (a), (b) and (c) contain the images reconstructed by use of the single-plane, half-scan and conventional I-DT algorithms, respectively. The images reconstructed by use of the conventional I-DT algorithm shown in figures 12(c) and 13(c) are both accurate reconstructions of $f(x, y)$. This is expected because the conventional I-DT algorithm does not assume that the object function is real valued. On the other hand, the images reconstructed by use of the single-plane algorithm, shown in figures 12(a) and 13(a), are both blurred dramatically, and no longer even remotely resemble the object and its background medium. The image reconstructed by use of the half-scan algorithm with $\lambda = 1 \times 10^{-3}$, shown in figure 12(b), contains certain horizontal streaking-like artefacts, but is of much better visual quality than the corresponding image reconstructed by

use of the single-plane algorithm. The image reconstructed by use of the half-scan algorithm with $\lambda = 1 \times 10^{-6}$, shown in figure 13(b), does not contain the streaking artefacts, and appears comparable in visual quality to the images reconstructed by use of the conventional I-DT algorithm. This improvement in the fidelity of the image reconstructed by use of the half-scan algorithm can be understood by noting that the imaging problem gets more 'Radon transform-like' as λ decreases. Indeed, as $\lambda \to 0$ the shifted Ewald sphere surfaces in Fourier space, over which equation (8) determines $\hat{F}$ on, reduce to planar surfaces and therefore measurements taken over the angular range $\phi \in [0, \pi)$ will completely determine $\hat{F}$.

These observations indicate that the half-scan reconstruction algorithm is much more robust to violations of the assumption that f is real valued than is the single-plane reconstruction algorithm. The single-plane algorithm employs equation (20) to determine $\hat{F}[u_r, \phi]$ for all $\phi \in [0, 2\pi)$. This equation, however, assumes the symmetry $\hat{F}[u_r, \phi] = \hat{F}^*[u_r, \phi^\pi]$ (which is valid only if f is real valued), so all the determined values of $\hat{F}$ will be incorrect when f is complex. In contrast, the half-scan algorithm uses equation (8) to determine $\hat{F}[u_r, \phi]$ for $\phi \in [0, \pi)$; this equation does not assume that f is real-valued and so these values of $\hat{F}[u_r, \phi]$ can be determined accurately even for complex f. Only the components corresponding to $\phi \in [\pi, 2\pi)$ are determined by the assumption that f is real valued, and so at least half of the Fourier data can be determined accurately in the half-scan algorithm. All of these discussions can be generalized immediately to address the 3D and spherical-wave phase I-DT problems.

6. Summary and conclusions

A new theory of I-DT has been proposed recently that permits for the reconstruction of the complex-valued refractive index distribution of a weak scatterer from knowledge of wavefield intensity measurements. At each tomographic view angle, I-DT requires the wavefield intensity to be measured on two parallel detector planes that are separated by a finite distance. In many imaging tasks in biology and materials science, the imaginary component of the refractive index distribution $n(\vec{r})$ of the scattering object may be approximately zero and such scattering objects are referred to as phase objects. Although the theory of I-DT permits for the reconstruction of phase objects, we can expect that the amount of measurement data needed to reconstruct a phase object will be less than that needed to reconstruct an complex-valued refractive index distribution. Reducing the amount of required measurement data has the obvious benefit of minimizing the experimental complexity of an I-DT imaging study, which in turn can minimize the probability of artefacts due to object motion (e.g., when imaging biological samples) and improve the efficiency of high-throughput imaging applications.

In this work, we developed and investigated two I-DT reconstruction algorithms for reconstruction of 3D phase objects that each utilize only half of the measurements that would be needed by a conventional I-DT reconstruction algorithm for reconstruction of an arbitrary complex-valued object function. The first algorithm, referred to as the *half-scan* algorithm, required that intensity measurements be acquired on two different measurement planes at a given view angle (as in conventional I-DT), but the tomographic scanning needed to cover only one-half of the full angular scanning range (e.g., over the range $[0, \pi)$ in the 2D case). The second algorithm, referred to as the *single-plane* algorithm, required that only one intensity measurement be acquired at a given view angle, but the tomographic scanning needed to cover the full angular scanning range (e.g., over the range $[0, 2\pi)$ in the 2D case). Both the half-scan and single-plane algorithms were generalized to accommodate spherical incident wavefields. Although the half-scan and single-plane reconstruction algorithms were equivalent mathematically, we demonstrated analytically and numerically that their resolution and noise

propagation properties can differ considerably, depending on the choice of the parameters of the scanning geometries.

We are currently performing a detailed investigation of the noise properties of reconstructed images in I-DT and their objective assessment, and will report this work in a future publication. Furthermore, we intend to evaluate I-DT reconstruction algorithms by use of experimental coherent x-ray and optical measurement data.

Acknowledgment

The corresponding author (MA) thanks Dr Xiaochuan Pan for stimulating discussions and his encouragement.

Appendix

Here we provide a derivation, which represents a specialized version of the 3D filtered backpropagation algorithm for reconstruction of a real-valued $f(\vec{r})$ from data acquired over a π angular range.

If $\hat{F}[u_r/\alpha^2, v_r/\alpha^2, \phi, 0]$ is known $\forall\phi \in [0, 2\pi)$, then an estimate of $f(\vec{r})$ can be obtained by use of the spherical-wave filtered backpropagation reconstruction algorithm (Lu 1985, Anastasio 2001) as

$$f(\vec{r}) = f_1(\vec{r}) + f_2(\vec{r}) \tag{A.1}$$

where

$$f_i(\vec{r}) = \frac{1}{2}\int_{A_i} \mathrm{d}\phi \int\int_{u_r^2+v_r^2 \leqslant \alpha^2 k^2} \mathrm{d}u_r\, \mathrm{d}v_r \frac{|u_r|}{\alpha^6 w_{\alpha,r}}[(1-\alpha^2)w_{\alpha,r} + \alpha^2 k] \times \hat{F}[u_r/\alpha^2, v_r/\alpha^2, \phi, 0] \exp\left(j\left(\frac{u_r}{\alpha^2}x_r + (w_{\alpha,r} - k)z_r + \frac{v_r}{\alpha^2}y_r\right)\right) \tag{A.2}$$

and, for $i = 1, 2$, the integration over ϕ is performed over the intervals

$$A_i = \begin{cases} [0, \pi) & : \quad i = 1 \\ [\pi, 2\pi) & : \quad i = 2. \end{cases}$$

By letting $\phi \to \phi + \pi$ in the expression for $f_2(\vec{r})$ and making use of equation (18), one finds that

$$f_2(\vec{r}) = f_1^*(\vec{r}). \tag{A.3}$$

The use of equation (A.3) in equation (A.1) yields

$$f(\vec{r}) = f_1(\vec{r}) + f_1^*(\vec{r}) = 2\,\mathrm{Re}\{f_1(\vec{r})\}. \tag{A.4}$$

References

Anastasio M 2001 Development and analysis of image reconstruction algorithms in diffraction tomography *PhD Thesis* The University of Chicago

Anastasio M and Pan X 2000 Computationally efficient and statistically robust image reconstruction in 3D diffraction tomography *J. Opt. Soc. Am.* A **17** 391–400

Anastasio M and Pan X 2003 An improved reconstruction algorithm for 3D diffraction tomography using spherical-wave sources *IEEE Trans. Biomed. Eng.* **50** 517–21

Barty A, Nugent K A, Roberts A and Paganin D 2000 Quantitative phase tomography *Opt. Commun.* **175** 329–36

Chen B and Stamnes J 1998 Validity of diffraction tomography based on the first-Born and first-Rytov approximations *Appl. Opt.* **37** 2996–3006

Cheng J and Han S 2001 Diffraction tomography reconstruction algorithms for quantitative imaging of phase objects *J. Opt. Soc. Am.* A **18** 1460–4

Devaney A 1982 A filtered backpropagation algorithm for diffraction tomography *Ultrason. Imaging* **4** 336–50

Devaney A 1983 Diffraction tomography *Inverse Methods in Electromagnetic Imaging* part 2 *(NATO ASI Series)* ed W M Boerner pp 1107–36

Devaney A 1985 Generalized projection-slice theorem for fan-beam diffraction tomography *Ultrason. Imaging* **7** 264–75

Devaney A 1989 The limited view problem in diffraction tomography *Inverse Problems* **5** 501

Devaney A 1992 Diffraction tomographic reconstruction from intensity data *IEEE Trans. Image Process.* **1** 221–8

Gbur G, Anastasio M, Huang Y and Shi D 2004 Spherical-wave intensity diffraction tomography *J. Opt. Soc. Am.* A submitted

Gbur G and Wolf E 2002a Diffration tomography without phase information *Opt. Lett.* **27** 1890–2

Gbur G and Wolf E 2002b Hybrid diffraction tomography without phase information *J. Opt. Soc. Am.* A **19** 2194–202

Gbur G and Wolf E 2002c The information content of the scattered intensity in diffraction tomography *Inform. Sci.* **162** 3–20

Lu Z 1985 Multidimensional structure diffraction tomography for varying object orientation through generalised scattered waves *Inverse Problems* **1** 339–56

Maleki M and Devaney A 1993 Phase-retrieval and intensity-only reconstruction algorithms for optical diffraction tomography *J. Opt. Soc. Am.* A **10** 1086–92

Mueller R, Kaveh M and Wade G 1979 Reconstructive tomography and applications to ultrasonics *Proc. IEEE* **67** 567–87

Nugent K A, Gureyev T E, Cookson D, Paganin D and Barnea Z 1996 Quantitative phase imaging using hard x-rays *Phys. Rev. Lett.* **77** 2961–4

Pan X 1998 A unified reconstruction theory for diffraction tomography with considerations of noise control *J. Opt. Soc. Am.* **15** 2312–26

Slaney M, Kak A C and Larsen L 1984 Limitations of imaging with first-order diffraction tomography *IEEE Trans. Microw. Theory Tech.* **32** 860–74

Spanne P, Raven C, Snigireva I and Snigirev A 1999 In-line holography and phase-contrast microtomography with high energy x-rays *Phys. Med. Biol.* **44** 741–50

Wheeden R L and Zygmund A 1977 *Measure and Integral: An Introduction to Real Analyisis* (New York: Marcel Dekker)

Wolf E 1969 Three-dimensional structure determination of semi-transparent objects from holographic data *Opt. Commun.* **1** 153–6